Letter

Electronic bonding transitions in oxide glass above two megabar pressures

Yong-Hyun Kim [1], Paul Chow [2], Yuming Xiao [2], Guoyin Shen [2] and Sung Keun Lee [1,3,*]

[1] *School of Earth and Environmental Sciences, Seoul National University, Seoul 08826, Korea*

[2] *HPCAT, X-Ray Science Division, Argonne National Laboratory, Argonne, Illinois 60439, USA*

[3] *Institute of Applied Physics, Seoul National University, Seoul 08826, Korea*

(Received 13 December 2023; revised 22 March 2024; accepted 6 May 2024; published 3 June 2024)

Inelastic x-ray scattering (IXS) of B_2O_3 glass up to ~2.2 Mbar reveals electronic bonding transitions in oxide glasses. B *K*-edge IXS identifies the high-energy feature above ~1.4 Mbar and a gradual increase in its intensity toward ~2.2 Mbar, indicating the formation of hypervalent boron via electron polarization to oxygen atoms. The pressure-driven high energy shifts in O *K*-edge IXS indicate pronounced electronic dispersion that increases upon densification of amorphous oxides above ~2 Mbar. The extent of the energy shifts and enhanced polarization correlate with increasing atomic radius of cation in oxide glass, establishing the role of cation radius in electronic structures of amorphous oxides under compression. The results elucidate the electronic mechanisms behind the *delayed* structural transformation in low-*Z* oxide glasses, where transitions to highly coordinated cations are hindered well above 1 Mbar, providing the origin of incompressibility of low-*Z* amorphous oxide under multi-Mbar compression.

DOI: 10.1103/PhysRevResearch.6.L022051

Compounds consisting of elements with low atomic numbers (i.e., low-*Z* elements; B, C, etc.) exhibit diverse electronic bonding natures, from the weakest interactions for molecular solids to the strongest covalent bonds for diamonds. Extreme compression of low-Z compounds at several Mbar (i.e., >100 GPa) modifies the atomic and electronic structures, inducing transitions in electronic bonds around low-Z element that are known to be rigid [1,2]. The electronic structures [e.g., electronic density of states (DOS)] at high pressure account for the pressure-driven changes in superionicity or superconductivity [3–5]. Bonding transitions in low-Z oxides at multi-Mbar provide insights into the behavior of light elements in oxide melts, governing the transport properties and isotopic fractionations in super-Earth's interiors [6–8].

Particularly, boron has three valence electrons ($2s^2\,2p^1$), displaying complex electronic bonding configurations [9–11]. B_2O_3 is the most stable oxide of boron with a tendency to form amorphous states. B_2O_3 glass (a-B_2O_3) comprises key constituents of technologically important glass-forming liquids. At 1 atm, a-B_2O_3 consists of the BO_3 units, which form the superstructural boroxol rings [12–14]. a-B_2O_3 undergoes coordination transformation from $^{[3]}$B to $^{[4]}$B above ~5 GPa, forming amorphous networks with sp^3 hybridization above ~20 GPa [15–19]. $^{[4]}$B prevails up to 1.2 Mbar, currently the highest pressure achieved for a-B_2O_3 from experimental studies [20]. The absence of the $^{[5]}$B formation above Mbar pressures distinguishes the a-B_2O_3 from other high-*Z* oxide glasses, such as SiO_2, GeO_2, and TeO_2, where the formation of $^{[5,6]}$Si, $^{[5,6,7]}$Ge, and $^{[6]}$Te governs the glass densification well below 1 Mbar [21–28]. Such *delayed* coordination transformations in low-*Z* glasses beyond 1 Mbar remain a puzzle.

Theoretical calculations predicted the post-$^{[4]}$B formation in crystalline and amorphous B_2O_3 toward multi-Mbar [29–33] [see SM1 in the Supplemental Material (SM) [34]]. Formation of hypervalent environments (i.e., $^{[5,6]}$B) may govern the glass densification at multi-Mbar [48–51]. Electronic structures of a-B_2O_3 beyond Mbar could provide insight into how light-element-bearing compounds modify the bonding natures to afford the structural densification [1,52], unveiling the origin of the delayed transitions in glasses. Despite the fundamental importance, probing of atomic and electronic structures for low-*Z* amorphous materials at multi-Mbar remains a challenge, due to experimental difficulties in the elastic x-ray scattering with small atomic scattering factors and/or in the x-ray spectroscopic probes with limited penetration depth of soft x rays (see SM2 [34] for the experimental challenges in probing the structure a-B_2O_3 and SM3 for the demonstration of the limitations in Raman spectroscopy of a-B_2O_3 above ~1 Mbar). Inelastic x-ray scattering (IXS) can uncover the electronic structures of low-*Z* elements above *megabar* pressures [16,41,53–58] (see SM4). Whereas B *K*-edge IXS has been the only successful probe in identifying pressure-induced increases in boron coordination numbers (CN_B) for borate glasses above ~50 GPa [16,20,59–61], pressure conditions have been limited to 1.2 Mbar. In this study, IXS with focused x rays and postcollimation optics [62] allows us to reveal the electronic structures of a-B_2O_3 at 2.2 Mbar, further expanding the capability of IXS above 200 GPa. The current results doubled the accessible pressure ranges of electronic structures around B in low-Z oxides, offering

*Corresponding author: sungklee@snu.ac.kr

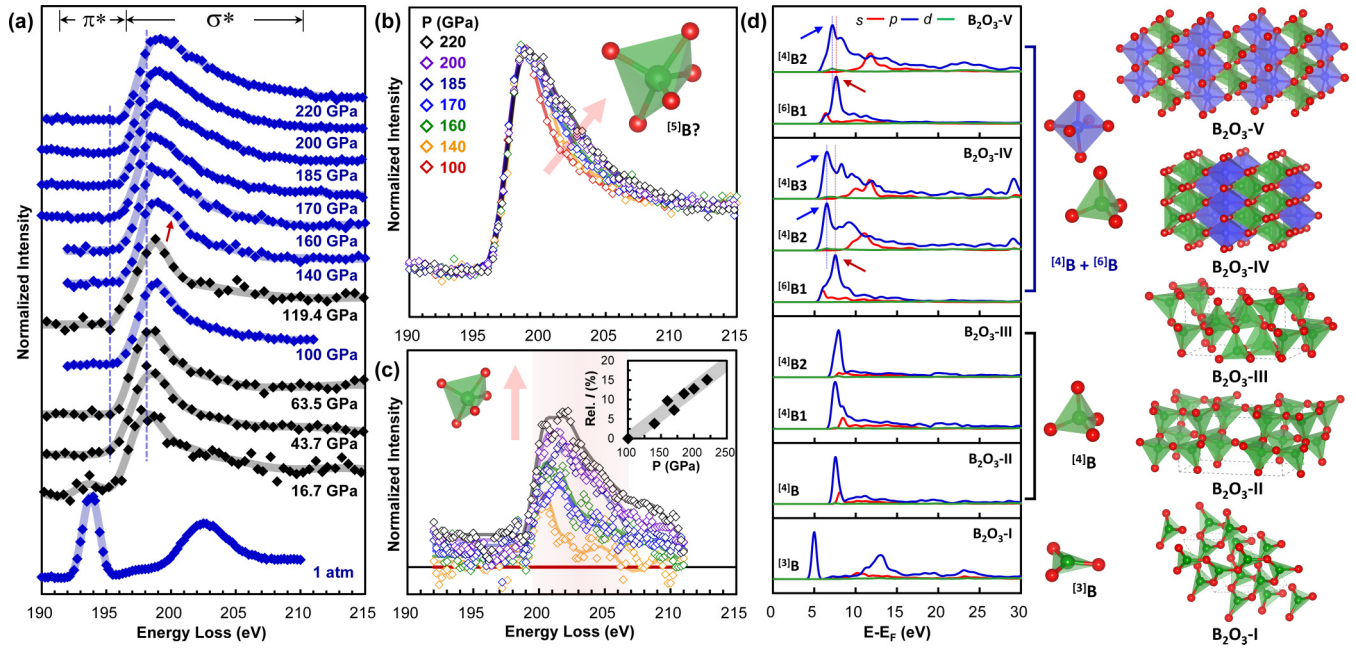

FIG. 1. (a) B *K*-edge IXS spectra for a-B_2O_3 up to ~220 GPa. The IXS spectra with black lines are from earlier studies [16,20]. (b) B *K*-edge IXS spectra and (c) difference IXS spectra for a-B_2O_3 above ~100 GPa. The difference spectra were calculated by subtracting the IXS spectrum at high pressure relative to 100 GPa. Inset shows the increase in the relative intensities of high-energy features. (d) Calculated *l*-resolved B PDOS for boron sites in B_2O_3 polymorphs. Crystal structures and boron environments are shown.

prospects for the explorations of electronic origins of high-T_c superconductors, metallization of insulators, or formation of electrides above Mbar conditions.

The *in situ* IXS spectra for a-B_2O_3 were collected at the 16-ID-D beamline of the Advanced Photon Source. The diamonds with culet diameters of 90–100 μm were used for pressure generation. The Raman signal of culet was used to estimate pressure conditions [63]. The monochromatic x rays were produced by Si(111) double crystals. IXS signals were collected with a polycapillary postsample collimator at the scattering angle of 25° [62], and analyzed with a spherical Si(555) crystal operating at 9.9067 keV. The IXS signals were collected by varying energy losses (see SM5 for experimental details). *Ab initio* calculations of the partial DOS for B_2O_3 crystals [32] were performed on the WIEN2K [64]. The Perdew-Burke-Ernzerhof functional was adopted for the exchange correlation [65]. The core-hole effects were addressed by the final state approximation [36,66] (see SM6 for computational details).

The B *K*-edge IXS spectra for a-B_2O_3 reveal the evolution of boron environments toward 2.2 Mbar [Fig. 1(a)]. At 1 atm, the IXS spectrum shows two features at ~194 and ~203 eV, corresponding to the excitation of B 1*s* electrons to π^* and σ^* antibonding orbitals of $^{[3]}$B, respectively [16,67,68]. While the descriptions of IXS spectra and densification mechanisms below ~1.2 Mbar are available [16,20], briefly, the feature at ~198 eV emerges upon compression, corresponding to $^{[4]}$B [67,68]. With a further compression toward ~1.2 Mbar, pressure-induced shifts of the main feature indicate the B-O bond length (d_{B-O}) reduction of ~0.05–0.08 Å [20]. Except for the shifts, no significant change in spectral shapes was observed, indicating the dominance of $^{[4]}$B up to 119.4 GPa [20]. Extended stability of $^{[4]}$B is contrast to other glass-forming oxides (e.g., SiO_2) with dramatic coordination transformations below Mbar [22–24].

Above 120 GPa, IXS spectra reveal the emergence of a spectral feature around ~200–204 eV. The feature remains prominent up to 220 GPa, and its intensity gradually builds up with increasing pressures [Figs. 1(b) and 1(c)]. The B *K*-edge spectrum broadens upon compression, partly because of a dispersion of electronic states above 1.4 Mbar. The spectral changes for B_2O_3 glass above ~1.4 Mbar are rather gradual and continuous; the IXS patterns suggest the gradual structural modification around the boron, such as CN_B and/or d_{B-O}, which is characteristic to the densification of amorphous oxides under compression. Earlier theoretical simulations predicted the $^{[5]}$B formation above ~140 GPa [29,33] (SM1). The high-energy features at ~200–204 eV may, thus, arise from an increase in the $^{[5]}$B fraction; other structural densifications, such as changes in the atomic configurations beyond the nearest neighbors can also affect the B *K*-edge features.

The B partial DOS (PDOS) for crystalline B_2O_3 up to 179 GPa was calculated to explore the origin of electronic transitions in a-B_2O_3 above ~1.4 Mbar [Fig. 1(d); see SM7 for the structure of B_2O_3 polymorphs]. Calculated results for B_2O_3-I to B_2O_3-III reproduce the PDOS characteristic to $^{[3]}$B and $^{[4]}$B. Above 133 and 179 GPa, the B_2O_3 crystals transform into B_2O_3-IV and B_2O_3-V phases with $^{[4]}$B and $^{[6]}$B (with relative fractions of 3:1 and 1:1) [32]. The results for $^{[4]}$B reveal a major feature at ~6 eV [blue arrows, Fig. 1(d)] with a shoulder at higher energy, due to a broadening of the *p* states around $^{[4]}$B. Electronic repulsions due to d_{B-O} reduction for $^{[4]}$B (i.e., from ~1.44 Å at 46 GPa to ~1.37 Å at 179 GPa) and close packing of BO_X polyhedra account for the pronounced delocalization of the *p* states. The spectral features for $^{[6]}$B at

~7 eV [red arrows, Fig. 1(d)] get rather sharp, indicating that an electronic dispersion is less prominent due to an elongation of d_{B-O} (e.g., ~1.39 Å and ~1.56 Å at 133 GPa for $^{[4]}$B and $^{[6]}$B, respectively). Notably, calculated B PDOS for B_2O_3 reveals a negligible contribution from *d* states, in contrast to SiO_2 at high pressures [25,35]. Formation of six B-O bonds in B_2O_3 crystals at Mbar violates the conventional octet rule, making $^{[6]}$B the hypervalent species [50]. One way to address the hypervalent $^{[6]}$B is the polarization of B-O bonds toward ionic, to alleviate the coordination constraints from the octet rule. Alternatively, multicenter bonds (i.e., electrons are delocalized over multiple atoms) facilitate the formation of $^{[6]}$B [1,2]; note that both models make use of electron transfer from boron to oxygen to describe the polarization (see O PDOS below for further discussion). This could result in a relatively narrow B PDOS patterns for $^{[6]}$B in crystalline borates. The *s* states also exhibit the distinct patterns for $^{[4,6]}$B (SM8).

B *K*-edge IXS features for *a*-B_2O_3 above 140 GPa [Figs. 1(a) and 1(c)] revealed the formation of high-energy feature at ~201 eV, with gradual increases in the relative intensities to ~15% at 2.2 Mbar [inset in Fig. 1(c)]. While the B *K*-edge IXS may not fully constrain the fraction of $^{[5]}$B (SM9), earlier theoretical simulations showed the $^{[5]}$B formation above ~1.4 Mbar with $^{[5]}$B fraction of ~10–25% at ~2 Mbar (SM1 and Fig. S1) [29–31,33]. The overall similarities in the pressure ranges and relative intensities of the high-energy feature may indicate that this feature can be attributed to $^{[5]}$B. Furthermore, the calculated B PDOS (i.e., *p* states) for B_2O_3 crystals showed the features at slightly higher energies for $^{[6]}$B, suggesting that high-energy IXS features could originate from an increase in CN_B. The increase in the intensity of high-energy feature [Fig. 1(c)] toward ~2.2 Mbar, thus, suggests the increase in the fraction of highly coordinated B by the *partial* transformation of $^{[4]}$B to $^{[5]}$B. Note that B_2O_3 crystals undergo post-$^{[4]}$B phase transformations at 1.33 Mbar (with average CN_B of ~4.5 above 133 GPa and ~5.0 above 179 GPa) [32]. The caution needs to be taken to infer the coordination environments of amorphous oxides from their crystalline counterparts, because crystalline B_2O_3 bypasses the formation of $^{[5]}$B [31]. Nevertheless, together with inputs from the earlier computational studies [29,33], the observed spectral patterns support the $^{[5]}$B formation in *a*-B_2O_3 above ~1.4 Mbar. The broadening of B *K*-edge features above ~2 Mbar, therefore, indicates the electronic delocalization around the compressed $^{[5]}$B. Note that the collective structural evolutions in borate networks (e.g., topological contraction involving the formation of pressure-driven dense atomic configurations both in short-range scale and beyond the nearest neighbors [20,35], accompanied by the $^{[5]}$B formation) should contribute to the spectral patterns above ~1.4 Mbar (see SM9 for the uncertainties in the structural interpretation of IXS patterns) and, thus, further studies are necessary to precisely constrain the atomic and electronic structures of $^{[5]}$B in *a*-B_2O_3. Finally, narrow B PDOS patterns for $^{[6]}$B [Fig. 1(d)] have been attributed to the polarization of electrons towards the oxygens and relaxation of *on-site* electronic repulsions (SM9); however, further theoretical studies are essential to establish the correlation of valence electron distributions and/or structural rearrangements with PDOS patterns.

Oxide densification involves the compact packing of oxygen, associated with an increase in the oxygen coordination number (CN_O) and a reduction in the O-O distances (d_{O-O}) [25]. The evolutions of oxygen environments upon the phase transformations of B_2O_3 crystals [Fig. 2(a), SM7] are manifested in the O PDOS [Fig. 2(b)]. The O PDOS of B_2O_3-I exhibits the sharp π^* feature at ~6 eV and broad σ^* feature at ~14 eV, characteristic to $^{[3]}$B –$^{[2]}$ O –$^{[3]}$ B. The O PDOS patterns of B_2O_3-II, with an oxygen tricluster ($^{[3]}$O1) and a bridging oxygen ($^{[2]}$O2), show substantially distinct electronic structures; the π^* feature vanishes in both $^{[2]}$O and $^{[3]}$O, indicating the removal of planar $^{[3]}$B and formation of $^{[4]}$B. The σ^* feature, observed around ~14 eV for B_2O_3-I, shifts toward ~10 eV for B_2O_3-II. In B_2O_3-III, PDOS features exhibit substantial broadening, corresponding to a reduction in the B-$^{[2]}$O-B angle and d_{O-O}. Note that O PDOS shows the contributions from both B-O bonds and nonbonding electrons (i.e., lone-pair electrons) (SM10), where the annihilation of lone-pair electrons accounts for the transformation of $^{[3]}$B to $^{[4]}$B [69,70]. The B_2O_3-IV phase consists of four $^{[3]}$O sites with corner- and edge-sharing morphologies of $^{[4]}$B and $^{[6]}$B. For B_2O_3-V, an increase in the $^{[6]}$B fraction leads to the formation of oxygen quadclusters ($^{[4]}$O) with an average CN_O of ~3.33. The PDOS patterns for B_2O_3-IV and -V phases show a broad distribution of electronic states, indicating the dispersion of electrons under elevated pressures. The formation of $^{[6]}$B further reduces d_{O-O} by decreasing the O-B-O angles, enhancing the spatial proximities and interactions among the oxygens [35,71].

The O PDOS for the crystalline B_2O_3 reveals a control of local oxygen environments [O-B bond lengths (d_{O-B}), d_{O-O}, and CN_O] on the bonding natures [Figs. 2(c) and 2(d)]. The spectral average (E_c; energy loss at the spectral center of gravity, see [35,36] for further details on the spectral quantifications and physical meaning of the E_c, and also see [20,25,26,37] for the spectral quantification of the experimental IXS features) was used to quantify the overall variation in the O PDOS of diverse crystalline and amorphous oxides [25,26,35]. Figure 2(c) shows that E_c decreases with increasing d_{O-B} for each oxygen environment, whereas the correlation does not hold when all coordination environments are taken into consideration. Figure 2(d) shows that E_c decreases with increasing d_{O-O}, consistent with our earlier studies on diverse oxides (e.g., SiO_2, GeO_2) [25,26,35,37].

The O *K*-edge IXS reveals the pressure-induced evolution of oxygen environments in *a*-B_2O_3 [Fig. 3(a)]. The IXS spectrum at 1 atm shows π^* and σ^* features at 536 and 545 eV, respectively, corresponding to $^{[3]}$B –$^{[2]}$O –$^{[3]}$B [Fig. 3(b)] [16]. The *K*-edge feature gradually transforms into the broad σ^* peak at 543 eV above ~22.5 GPa, forming $^{[3]}$O [16,20]. At ~101.6 GPa, the IXS spectrum shifts to ~545 eV with a noticeable broadening of the *K*-edge feature, increasing the spectral intensity at ~547 eV [red vertical zone in Fig. 3(a)] [16,20]. Above ~140 GPa, O *K*-edge IXS spectra show a further increase in the spectral intensity above ~550 eV [around ~555 eV; blue vertical zone in Fig. 3(a)]. The increase in the dispersion of PDOS for *a*-B_2O_3 above ~140 GPa arises from electron transfer from $^{[5]}$B to oxygens, which may increase the effective charges of oxygen and electronic interactions among

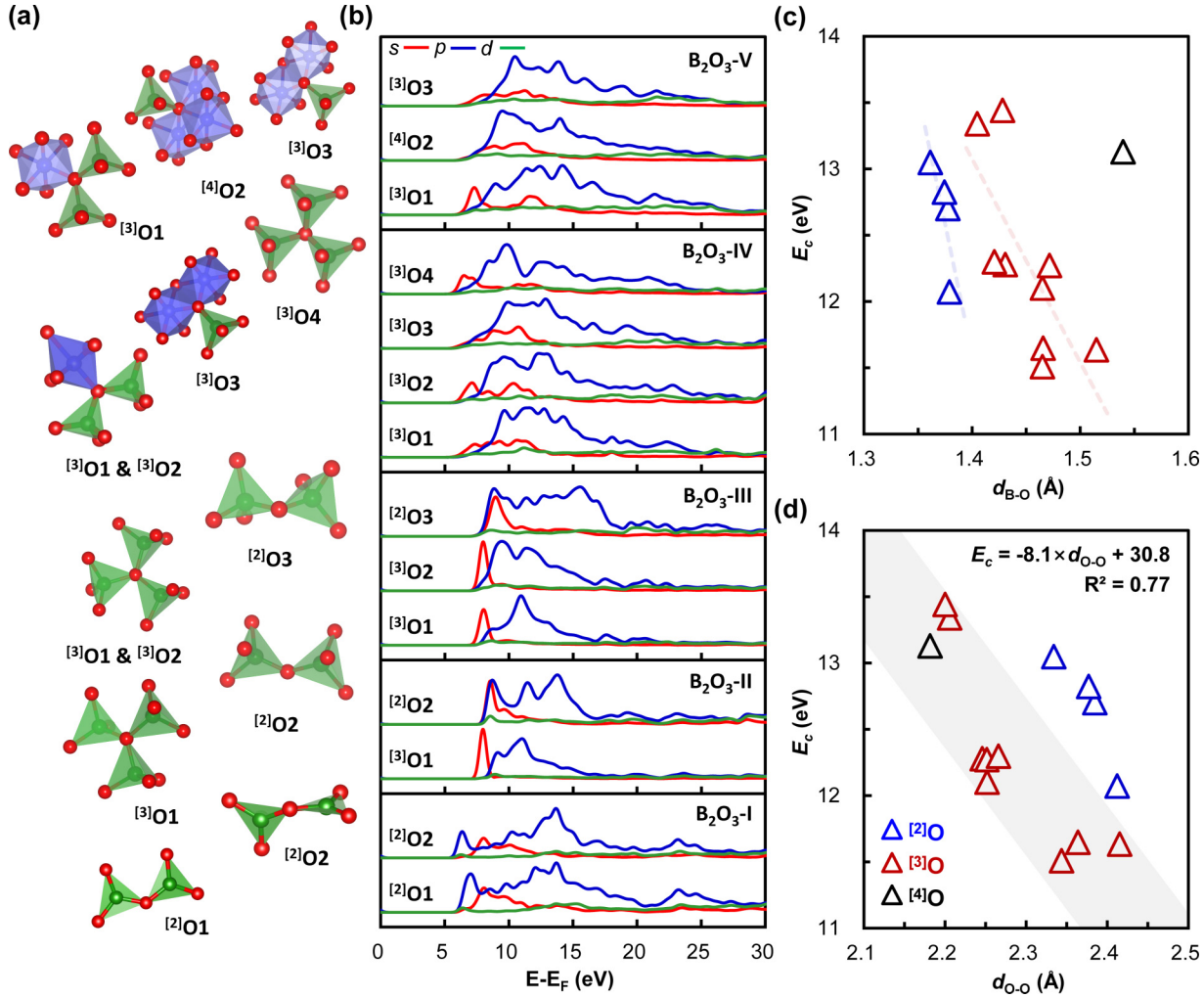

FIG. 2. (a) Local oxygen environments in B_2O_3 polymorphs at high pressure. (b) Calculated l-resolved O PDOS for each oxygen crystalline morphology. The E_c for B_2O_3 crystals with varying (c) d_{B-O} and (d) d_{O-O}. Blue, red, and black triangles show E_c for $^{[2]}$O, $^{[3]}$O, and $^{[4]}$O, respectively.

oxygens to broaden the O K-edge IXS features. Such pressure-driven broadening also indicates an increase in B-O-B bond angle variations and d_{O-O} distributions, which is prevalent in oxide glasses at high pressure [20,25,72–77]. Based on the correlation between E_c and d_{O-O} [Fig. 2(d)], the observed shifts in E_c up to 220 GPa indicate the d_{O-O} reduction of ∼0.6–0.7 Å.

The E_c for crystalline oxides shows a linear correlation with d_{O-O} [Fig. 4(a)], consistent with earlier reports for SiO_2 and GeO_2 at high pressure [25,26,35–37]: $E_c = -11.1 \times d_{O-O} + 569.48$. While correlations may vary with composition and types of oxides (e.g., $E_c = -12.9 \times d_{O-O} + 574.9$ for SiO_2 [35] and $E_c = -9.6 \times d_{O-O} + 565.5$ for GeO_2 [26]), a current linear trend could be useful to predict the pressure-induced changes in d_{O-O} for diverse oxide crystals well above 2 Mbar ($R^2 = 0.95$). Figure 4(b) shows that E_c for *amorphous* oxides shifts toward the higher energies upon compression, due to the d_{O-O} reduction at high pressures (SM11). At 1 atm, E_c ranges from ∼537.4 eV for GeO_2 to ∼542.4 eV for B_2O_3, due to the ∼0.45 Å shorter average d_{O-O} for B_2O_3, consistent with earlier experimental results (i.e., d_{O-O} of ∼2.40 Å and ∼2.83 Å for B_2O_3 [78] and GeO_2 [79], respectively). Figure 4(c) shows pressure-driven shifts in E_c ($\Delta E_c = E_{c,P} - E_{c,1\,atm}$) of oxide glasses at high pressure. At a given pressure, ΔE_c for a-B_2O_3 are smaller than others, indicating the less efficient d_{O-O} reduction for a-B_2O_3 at high pressure (SM11); the ΔE_c for a-B_2O_3 at ∼1.5 Mbar is ∼4.7 eV (Δd_{O-O} of ∼0.42 Å), while the ΔE_c for GeO_2 is ∼5.6 eV (Δd_{O-O} of ∼0.51 Å) at ∼1.5 Mbar. Notably, ΔE_c for oxide glass at given pressure condition increases with increasing atomic radii of cations (i.e., ∼0.85 Å, ∼1.10 Å, ∼1.25 Å for B, Si, Ge at 1 atm, respectively). The results show the pivotal role of atomic radius of a cation on the spectral PDOS patterns and densification of oxides above multi-Mbar. The absence of d states in the a-B_2O_3 further hinders the structural rearrangements upon densification, because the d states in SiO_2, GeO_2, and TeO_2 glasses can promote the more substantial pressure-induced changes in d_{O-O} by forming highly coordinated $^{[5,6]}$Si, $^{[5,6,7]}$Ge, and $^{[6]}$Te via $sp^3\,d^2$ hybridization [28,80]. Such *electronic* contributions to the structural hindrance may account for the increase in the pressure conditions to the coordination transformation in low-Z oxide glass [20].

Bonding transitions in a-B_2O_3 under extreme pressures indicate the prevalence of highly coordinated B in melts in

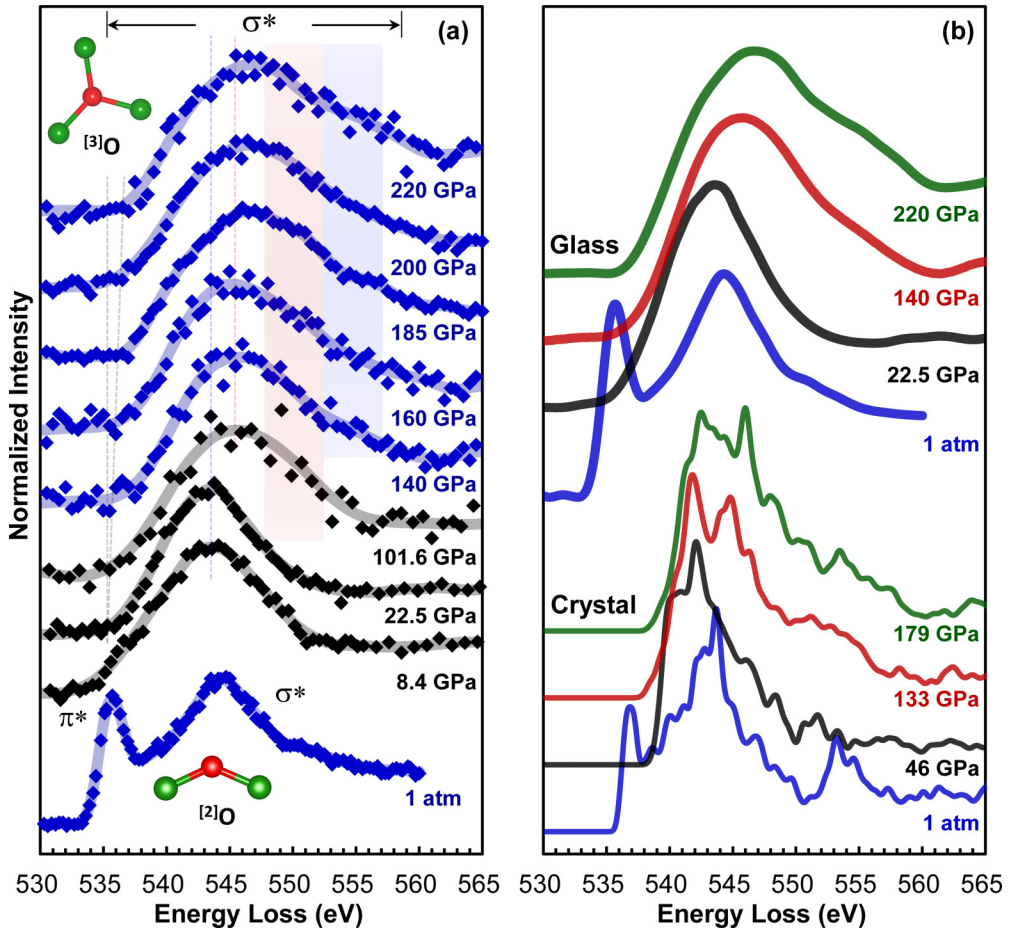

FIG. 3. (a) O *K*-edge IXS spectra for a-B_2O_3 up to ~220 GPa. The IXS spectra below ~100 GPa were reported in our earlier studies [16,20]. Red and blue vertical zones highlight the increase in the spectral intensity at ~547 eV and ~555 eV above ~100 GPa and ~140 GPa, respectively. (b) O *K*-edge IXS spectra for crystalline and a-B_2O_3 at high pressure. The spectra for B_2O_3 polymorphs were calculated by averaging the O PDOS of oxygen sites in crystals.

planetary interior under multi-Mbar pressure [6,7,81,82]. The chemical behavior of boron (i.e., isotope fractionation) in melts has been a proxy to the recycling of subducting slabs and magmatism in Earth [83,84]. Enrichment of ^{10}B in melts arises from the preferential incorporation of ^{10}B into $^{[4]}B$, where an increase in the $^{[4]}B$ fraction at high pressure reduces the $^{11}B/^{10}B$ ratios of magma at depth [85,86]. Prevalence of $^{[4]}B$ up to ~1.2 Mbar suggests the ^{10}B enrichment in Earth's lower mantle melts [20]. The formation of $^{[5,6]}B$ at multi-Mbar further promotes the tendency to enrich ^{10}B for oxide melts, making the isotope signals of super-Earth's mantle melts to be largely different from those of Earth's.

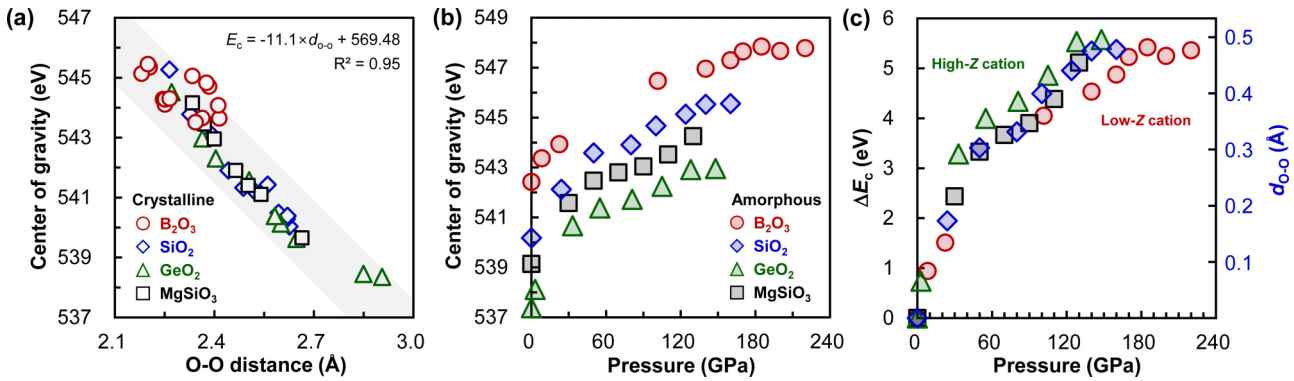

FIG. 4. (a) E_c for crystalline oxides with varying d_{O-O}. (b) E_c and (c) shifts in the E_c (ΔE_c) for amorphous oxides with increasing pressures. The E_c for B_2O_3, SiO_2, GeO_2, and $MgSiO_3$ are shown with red, blue, green, and black symbols. The E_c values for SiO_2, GeO_2, and $MgSiO_3$ crystals and glasses are retrieved from our earlier studies [20,26,35–37].

Finally, the electronic structures of oxides are essential to unveil the origin of glass densification. Current study reports the first electronic DOS of oxide glass above ∼2 Mbar. Whereas the prevalence of $^{[4]}$B in a-B_2O_3 up to ∼1.2 Mbar remains a puzzle, the B K-edge IXS above ∼1.4 Mbar demonstrates the evolution of boron PDOS upon the formation of hypervalent B, where electron transfer from boron to oxygen may account for the formation of highly coordinated B. O PDOS reveals the dispersion of electronic state in both crystalline and a-B_2O_3 above ∼1.4 Mbar. The electron transfer and an increase in effective charge around oxygen accompanied by the hypervalent B can account for the observed electronic dispersion. This enhanced polarization is expected to be a common feature for other low-Z (e.g., second-row elements) glasses or crystals under extreme pressure, elucidating the mechanisms behind delayed transformation and densification paths under multi-Mbar conditions. The O K-edge IXS spectra for a-B_2O_3 further corroborate the effect of d_{O-O} on E_c above 2 Mbar. The ΔE_c for oxide glasses increases with increasing atomic radius of cations; the ΔE_c for a-B_2O_3, low-Z oxides, is smaller than other oxides. The DOS-based densification model opens a window to predict the transition path in various condensed matters under pressure. As a low-Z material under compression is much less compressible, the systematic ΔE_c differences in diverse oxide glasses account for why low-Z glass exhibits greater incompressibility compared to high-Z glass. Our IXS study exceeds the highest pressure conditions for glasses using elastic x ray. Considering several orders of magnitude weaker IXS signal than elastic x-ray signal, current progress constitutes major experimental advancements. IXS gains widespread use in upgraded and newly constructed synchrotron sources. The IXS results with the electronic DOS up to ∼2.2 Mbar, thus, sheds light on extensive pursuits of novel electronic behaviors of materials under multi-Mbar compression.

This work was supported by the Research Leader program of National Research Foundation of Korea (NRF) Grant No. NRF-2020R1A3B2079815 to S.K.L. Y.-H.K. acknowledges the support by the Global Ph.D. Fellowship Program of the NRF Grant funded by Korean Government (Grant No. NRF-2017H1A2A1042446). Portions of this work were performed at the HPCAT, Advanced Photon Source (APS), Argonne National Laboratory (ANL). HPCAT operations are supported by DOE-NNSA's Office of Experimental Sciences. The APS is a user facility operated for the DOE Office of Science by ANL under Contract No. DE-AC02-06CH11357. We thank the reviewers for constructive comments and inputs, which improved the manuscript's quality and clarity.

[1] W. Grochala, R. Hoffmann, J. Feng, and N. W. Ashcroft, The chemical imagination at work in very tight places, Angew. Chem. Int. Ed. **46**, 3620 (2007).

[2] C.-S. Yoo, Chemistry under extreme conditions: Pressure evolution of chemical bonding and structure in dense solids, Matter Radiat. Extrem. **5**, 018202 (2020).

[3] X.-J. Chen, V. V. Struzhkin, Y. Yu, A. F. Goncharov, C.-T. Lin, H.-k. Mao, and R. J. Hemley, Enhancement of superconductivity by pressure-driven competition in electronic order, Nature (London) **466**, 950 (2010).

[4] Y. He, S. Sun, D. Y. Kim, B. G. Jang, H. Li, and H.-k. Mao, Superionic iron alloys and their seismic velocities in Earth's inner core, Nature (London) **602**, 258 (2022).

[5] C. Ji *et al.*, Ultrahigh-pressure isostructural electronic transitions in hydrogen, Nature (London) **573**, 558 (2019).

[6] D. E. Fratanduono, M. Millot, R. G. Kraus, D. K. Spaulding, G. W. Collins, P. M. Celliers, and J. H. Eggert, Thermodynamic properties of $MgSiO_3$ at super-Earth mantle conditions, Phys. Rev. B **97**, 214105 (2018).

[7] S. K. Bajgain, A. W. Ashley, M. Mookherjee, D. B. Ghosh, and B. B. Karki, Insights into magma ocean dynamics from the transport properties of basaltic melt, Nat. Commun. **13**, 7590 (2022).

[8] J. Liu, Q. Hu, W. Bi, L. Yang, Y. Xiao, P. Chow, Y. Meng, V. B. Prakapenka, H.-K. Mao, and W. L. Mao, Altered chemistry of oxygen and iron under deep Earth conditions, Nat. Commun. **10**, 153 (2019).

[9] S. Mondal *et al.*, Electron-deficient and polycenter bonds in the high-pressure γ-B_{28} phase of boron, Phys. Rev. Lett. **106**, 215502 (2011).

[10] F. Peng, M. Miao, H. Wang, Q. Li, and Y. Ma, Predicted lithium–boron compounds under high pressure, J. Am. Chem. Soc. **134**, 18599 (2012).

[11] Q. Chen, H. Lu, H.-J. Zhai, and S.-D. Li, Chemical bonding in electron-deficient boron oxide clusters: Core boronyl groups, dual 3c–4e hypervalent bonds, and rhombic 4c–4e bonds, Phys. Chem. Chem. Phys. **16**, 7274 (2014).

[12] A. C. Wright, My borate life: An enigmatic journey, Int. J. Appl. Glass Sci. **6**, 45 (2015).

[13] J. Wu and J. F. Stebbins, Cation field strength effects on boron coordination in binary borate glasses, J. Am. Ceram. Soc. **97**, 2794 (2014).

[14] G. Ferlat, M. Hellgren, F.-X. Coudert, H. Hay, F. Mauri, and M. Casula, van der Waals forces stabilize low-energy polymorphism in B_2O_3: Implications for the crystallization anomaly, Phys. Rev. Mater. **3**, 063603 (2019).

[15] A. Zeidler *et al.*, Density-driven structural transformations in B_2O_3 glass, Phys. Rev. B **90**, 024206 (2014).

[16] S. K. Lee, P. J. Eng, H.-k. Mao, Y. Meng, M. Newville, M. Y. Hu, and J. Shu, Probing of bonding changes in B_2O_3 glasses at high pressure with inelastic X-ray scattering, Nat. Mater. **4**, 851 (2005).

[17] S. K. Lee, K. Mibe, Y. Fei, G. D. Cody, and B. O. Mysen, Structure of B_2O_3 glass at high pressure: A ^{11}B solid-state NMR study, Phys. Rev. Lett. **94**, 165507 (2005).

[18] G. Carini, A. Bartolotta, G. Di Marco, B. Fazio, M. Federico, V. Romano, G. Carini, and G. D'Angelo, Polyamorphism and liquid-liquid phase transition in B_2O_3, Phys. Rev. B **105**, 014105 (2022).

[19] X. Jiang, M. S. Molokeev, N. Wang, Y. Wang, T. Wen, Z. Dong, Y. Liu, W. Li, and Z. Lin, sp^2 to sp^3 hybridization transformation in ionic crystals under unprecedentedly low pressure, Angew. Chem. Int. Ed. **61**, e202208247 (2022).

[20] S. K. Lee, Y.-H. Kim, P. Chow, Y. Xiao, C. Ji, and G. Shen, Amorphous boron oxide at megabar pressures via inelastic

X-ray scattering, Proc. Natl. Acad. Sci. USA **115**, 5855 (2018).

[21] A. Zeidler, P. S. Salmon, and L. B. Skinner, Packing and the structural transformations in liquid and amorphous oxides from ambient to extreme conditions, Proc. Natl. Acad. Sci. USA **111**, 10045 (2014).

[22] Y. Kono, C. Kenney-Benson, D. Ikuta, Y. Shibazaki, Y. Wang, and G. Shen, Ultrahigh-pressure polyamorphism in GeO_2 glass with coordination number >6, Proc. Natl. Acad. Sci. USA **113**, 3436 (2016).

[23] Y. Kono, Y. Shu, C. Kenney-Benson, Y. Wang, and G. Shen, Structural evolution of SiO_2 glass with Si coordination number greater than 6, Phys. Rev. Lett. **125**, 205701 (2020).

[24] C. Prescher, V. B. Prakapenka, J. Stefanski, S. Jahn, L. B. Skinner, and Y. Wang, Beyond sixfold coordinated Si in SiO_2 glass at ultrahigh pressures, Proc. Natl. Acad. Sci. USA **114**, 10041 (2017).

[25] S. K. Lee, Y.-H. Kim, Y. S. Yi, P. Chow, Y. Xiao, C. Ji, and G. Shen, Oxygen quadclusters in SiO_2 glass above megabar pressures up to 160 GPa revealed by X-ray Raman scattering, Phys. Rev. Lett. **123**, 235701 (2019).

[26] Y.-H. Kim, Y. S. Yi, H.-I. Kim, P. Chow, Y. Xiao, G. Shen, and S. K. Lee, Pressure-driven changes in the electronic bonding environment of GeO_2 glass above megabar pressures, J. Am. Chem. Soc. **144**, 10025 (2022).

[27] S. S. Lobanov, S. Speziale, B. Winkler, V. Milman, K. Refson, and L. Schifferle, Electronic, structural, and mechanical properties of SiO_2 glass at high pressure inferred from its refractive index, Phys. Rev. Lett. **128**, 077403 (2022).

[28] A. G. Papadopoulos, N. S. Tagiara, E. Stavrou, F. Li, G. Yang, and E. I. Kamitsos, Pressure-induced structural transformations and electronic transitions in TeO_2 glass by Raman spectroscopy, J. Phys. Chem. Lett. **14**, 387 (2023).

[29] K. Trachenko, V. V. Brazhkin, G. Ferlat, M. T. Dove, and E. Artacho, First-principles calculations of structural changes in B_2O_3 glass under pressure, Phys. Rev. B **78**, 172102 (2008).

[30] V. V. Brazhkin, Y. Katayama, K. Trachenko, O. B. Tsiok, A. G. Lyapin, E. Artacho, M. Dove, G. Ferlat, Y. Inamura, and H. Saitoh, Nature of the structural transformations in B_2O_3 glass under high pressure, Phys. Rev. Lett. **101**, 035702 (2008).

[31] A. Vegiri and E. I. Kamitsos, Pressure-induced structural transformations in glass $0.3Li_2O$-$0.7B_2O_3$: A molecular dynamics study, Phys. Rev. B **82**, 054114 (2010).

[32] H. Dong, A. R. Oganov, V. V. Brazhkin, Q. Wang, J. Zhang, M. M. Davari Esfahani, X.-F. Zhou, F. Wu, and Q. Zhu, Boron oxides under pressure: Prediction of the hardest oxides, Phys. Rev. B **98**, 174109 (2018).

[33] S. Ohmura and F. Shimojo, *Ab initio* molecular-dynamics study of structural, bonding, and dynamic properties of liquid B_2O_3 under pressure, Phys. Rev. B **81**, 014208 (2010).

[34] See Supplemental Material at http://link.aps.org/supplemental/10.1103/PhysRevResearch.6.L022051 for the summary of the earlier experimental and theoretical studies of a-B_2O_3 at high pressures, *insitu* Raman spectroscopy of a-B_2O_3 up to ∼1.65 Mbar, experimental and computational methods, structural details of B_2O_3 crystals, structural interpretations of IXS patterns with potential uncertainties, and additional information of PDOS for B_2O_3 crystals, which includes Refs. [35,38–40,42–47,87].

[35] Y. S. Yi, H. Khim, Y.-H. Kim, and S. K. Lee, Spectral proxies for bonding transitions in SiO_2 and $MgSiO_3$ polymorphs at high pressure up to 270 GPa by O K-edge x-ray Raman scattering, Phys. Rev. B **103**, 214109 (2021).

[36] Y. S. Yi and S. K. Lee, Atomistic origins of pressure-induced changes in the O K-edge x-ray Raman scattering features of SiO_2 and $MgSiO_3$ polymorphs: Insights from ab initio calculations, Phys. Rev. B **94**, 094110 (2016).

[37] Y.-H. Kim, Y. S. Yi, H.-I. Kim, P. Chow, Y. Xiao, G. Shen, and S. K. Lee, Structural transitions in $MgSiO_3$ glasses and melts at the core-mantle boundary observed *via* inelastic X-ray scattering, Geophys. Res. Lett. **46**, 13756 (2019).

[38] S. K. Lee, Effect of pressure on structure of oxide glasses at high pressure: Insights from solid-state NMR of quadrupolar nuclides, Solid State Nucl. Magn. Reson. **38**, 45 (2010).

[39] M. Grimsditch, A. Polian, and A. C. Wright, Irreversible structural changes in vitreous B_2O_3 under pressure, Phys. Rev. B **54**, 152 (1996).

[40] J. Nicholas, S. Sinogeikin, J. Kieffer, and J. Bass, Spectroscopic evidence of polymorphism in vitreous B_2O_3, Phys. Rev. Lett. **92**, 215701 (2004).

[41] S. K. Lee, P. J. Eng, and H. K. Mao, in *Spectroscopic Methods in Mineralogy and Materials Sciences*, edited by G. S. Henderson, D. R. Neuville, and R. T. Downs (Mineralogical Society of America, Washington, DC, 2014), pp. 139–174.

[42] M. I. Eremets, Megabar high-pressure cells for Raman measurements, J. Raman Spectrosc. **34**, 515 (2003).

[43] S. K. Sharma, B. Simons, and J. F. Mammone, Relationship between density, refractive index and structure of B_2O_3 glasses at low and high pressures, J. Non-Cryst. Solids **42**, 607 (1980).

[44] T. Yano, N. Kunimine, S. Shibata, and M. Yamane, Structural investigation of sodium borate glasses and melts by Raman spectroscopy.: I. Quantitative evaluation of structural units, J. Non-Cryst. Solids **321**, 137 (2003).

[45] A. K. Hassan, L. M. Torell, L. Börjesson, and H. Doweidar, Structural changes of B_2O_3 through the liquid-glass transition range: A Raman-scattering study, Phys. Rev. B **45**, 12797 (1992).

[46] B. N. Meera and J. Ramakrishna, Raman spectral studies of borate glasses, J. Non-Cryst. Solids **159**, 1 (1993).

[47] M. N. Svenson, M. Guerette, L. Huang, and M. M. Smedskjaer, Raman spectroscopy study of pressure-induced structural changes in sodium borate glass, J. Non-Cryst. Solids **443**, 130 (2016).

[48] D. Kurzydłowski and P. Zaleski-Ejgierd, Hexacoordinated nitrogen(V) stabilized by high pressure, Sci. Rep. **6**, 36049 (2016).

[49] E. Magnusson, Hypercoordinate molecules of second-row elements: D functions or d orbitals? J. Am. Chem. Soc. **112**, 7940 (1990).

[50] D. Y. Lee and J. C. Martin, Compounds of pentacoordinate (10-B-5) and hexacoordinate (12-B-6) hypervalent boron, J. Am. Chem. Soc. **106**, 5745 (1984).

[51] T. H. Lee and S. R. Elliott, Hypervalency in amorphous chalcogenides, Nat. Commun. **13**, 1458 (2022).

[52] C. Lu, M. Miao, and Y. Ma, Structural evolution of carbon dioxide under high pressure, J. Am. Chem. Soc. **135**, 14167 (2013).

[53] S. K. Lee, Y. Yi, Y.-H. Kim, H.-i. Kim, P. Chow, Y. Xiao, P. Eng, and G. Shen, Imaging of the electronic bonding of diamond at

pressures up to 2 million atmospheres, Sci. Adv. **9**, eadg4159 (2023).

[54] U. Bergmann, D. Nordlund, P. Wernet, M. Odelius, L. G. M. Pettersson, and A. Nilsson, Isotope effects in liquid water probed by x-ray Raman spectroscopy, Phys. Rev. B **76**, 024202 (2007).

[55] A. Bommannavar *et al.*, Overview of HPCAT and capabilities for studying minerals and various other materials at high-pressure conditions, Phys. Chem. Miner. **49**, 36 (2022).

[56] Y. Q. Cai *et al.*, Ordering of hydrogen bonds in high-pressure low-temperature H_2O, Phys. Rev. Lett. **94**, 025502 (2005).

[57] W. L. Mao, H.-k. Mao, Y. Meng, P. J. Eng, M. Y. Hu, P. Chow, Y. Q. Cai, J. Shu, and R. J. Hemley, X-ray-induced dissociation of H_2O and formation of an O_2-H_2 alloy at high pressure, Science **314**, 636 (2006).

[58] P. Wernet *et al.*, The structure of the first coordination shell in liquid water, Science **304**, 995 (2004).

[59] S. K. Lee, P. J. Eng, H.-k. Mao, Y. Meng, and J. Shu, Structure of alkali borate glasses at high pressure: B and Li *K*-edge inelastic X-ray scattering study, Phys. Rev. Lett. **98**, 105502 (2007).

[60] S. K. Lee, P. J. Eng, H.-k. Mao, and J. Shu, Probing and modeling of pressure-induced coordination transformation in borate glasses: Inelastic x-ray scattering study at high pressure, Phys. Rev. B **78**, 214203 (2008).

[61] G. Lelong, L. Cormier, L. Hennet, F. Michel, J.-P. Rueff, J. M. Ablett, and G. Monaco, Lithium borates from the glass to the melt: A temperature-induced structural transformation viewed from the boron and oxygen atoms, Inorg. Chem. **60**, 798 (2021).

[62] P. Chow, Y. M. Xiao, E. Rod, L. G. Bai, G. Y. Shen, S. Sinogeikin, N. Gao, Y. Ding, and H. K. Mao, Focusing polycapillary to reduce parasitic scattering for inelastic x-ray measurements at high pressure, Rev. Sci. Instrum. **86**, 072203 (2015).

[63] Y. Akahama and H. Kawamura, Diamond anvil Raman gauge in multimegabar pressure range, High Press. Res. **27**, 473 (2007).

[64] P. Blaha, K. Schwarz, F. Tran, R. Laskowski, G. K. H. Madsen, and L. D. Marks, WIEN2k: An APW+lo program for calculating the properties of solids, J. Chem. Phys. **152**, 074101 (2020).

[65] J. P. Perdew, A. Ruzsinszky, G. I. Csonka, O. A. Vydrov, G. E. Scuseria, L. A. Constantin, X. Zhou, and K. Burke, Restoring the density-gradient expansion for exchange in solids and surfaces, Phys. Rev. Lett. **100**, 136406 (2008).

[66] C. Hébert, Practical aspects of running the WIEN2k code for electron spectroscopy, Micron **38**, 12 (2007).

[67] D. Li, G. M. Bancroft, and M. E. Fleet, B K-edge XANES of crystalline and amorphous inorganic materials, J. Electron Spectrosc. Relat. Phenom. **79**, 71 (1996).

[68] M. E. Fleet and X. Liu, Boron K-edge XANES of boron oxides: Tetrahedral B–O distances and near-surface alteration, Phys. Chem. Miner. **28**, 421 (2001).

[69] M. A. Salvadó, P. Pertierra, A. Morales-García, J. M. Menéndez, and J. M. Recio, Understanding chemical changes across the α-cristobalite to stishovite transition path in silica, J. Phys. Chem. C **117**, 8950 (2013).

[70] T. M. Muscenti, G. V. Gibbs, and D. F. Cox, A simple chemical view of relaxations at stoichiometric (110) surfaces of rutile-structure type oxides: A first-principles study of stishovite, SiO_2, Surf. Sci. **594**, 70 (2005).

[71] J.-F. Lin *et al.*, Electronic bonding transition in compressed SiO_2 glass, Phys. Rev. B **75**, 012201 (2007).

[72] S. K. Lee, J.-H. Parq, Y. S. Yi, S. Lee, H.-I. Kim, S.-M. Lee, and J. Yu, Structure and disorder in $MgSiO_3$ glasses above megabar pressures via nuclear magnetic resonance: DFT calculations, J. Am. Ceram. Soc. **105**, 5151 (2022).

[73] S. Li, J. J. Kweon, S. Lee, A. C. Lee, and S. K. Lee, Coordination changes in densified aluminate glass upon compression up to 65 GPa: A view from solid-state nuclear magnetic resonance, J. Phys. Chem. Lett. **14**, 2078 (2023).

[74] P. S. Salmon and A. Zeidler, Ordering on different length scales in liquid and amorphous materials, J. Stat. Mech. (2019) 114006.

[75] P. S. Salmon, A. Zeidler, M. Shiga, Y. Onodera, and S. Kohara, Ring compaction as a mechanism of densification in amorphous silica, Phys. Rev. B **107**, 144203 (2023).

[76] S. K. Lee, A. C. Lee, and J. J. Kweon, Probing medium-range order in oxide glasses at high pressure, J. Phys. Chem. Lett. **12**, 1330 (2021).

[77] X. Zhang *et al.*, Pressure-induced nonmonotonic cross-over of steady relaxation dynamics in a metallic glass, Proc. Natl. Acad. Sci. USA **120**, e2302281120 (2023).

[78] W. Soppe, C. van der Marel, W. F. van Gunsteren, and H. W. den Hartog, New insights into the structure of B_2O_3 glass, J. Non-Cryst. Solids **103**, 201 (1988).

[79] P. S. Salmon, A. C. Barnes, R. A. Martin, and G. J. Cuello, Structure of glassy GeO_2, J. Phys.: Condens. Matter **19**, 415110 (2007).

[80] Y. Hu, B. Kiefer, C. R. Bina, D. Zhang, and P. K. Dera, High-pressure γ-$CaMgSi_2O_6$: Does penta-coordinated silicon exist in the Earth's mantle? Geophys. Res. Lett. **44**, 11 (2017).

[81] N. V. Solomatova and R. Caracas, Pressure-induced coordination changes in a pyrolitic silicate melt from *ab initio* molecular dynamics simulations, J. Geophys. Res. **124**, 11232 (2019).

[82] M. Millot, N. Dubrovinskaia, A. Černok, S. Blaha, L. Dubrovinsky, D. G. Braun, P. M. Celliers, G. W. Collins, J. H. Eggert, and R. Jeanloz, Shock compression of stishovite and melting of silica at planetary interior conditions, Science **347**, 418 (2015).

[83] P. M. Kowalski and B. Wunder, in *Boron Isotopes: The Fifth Element*, edited by H. Marschall and G. Foster (Springer International Publishing, Cham, 2018), pp. 33–69.

[84] P. M. Kowalski, B. Wunder, and S. Jahn, *Ab initio* prediction of equilibrium boron isotope fractionation between minerals and aqueous fluids at high *P* and *T*, Geochim. Cosmochim. Acta **101**, 285 (2013).

[85] A. C. Lee, E. J. Kim, and S. K. Lee, Pressure-induced structural evolution in boron-bearing model rhyolitic glasses under compression: Implications for boron isotope compositions and properties of deep melts in Earth's interior, Geochim. Cosmochim. Acta **332**, 220 (2022).

[86] A. C. Lee and S. K. Lee, Network polymerization and cation coordination environments in boron-bearing rhyolitic melts: Insights from ^{17}O, ^{11}B, and ^{27}Al solid-state NMR of sodium aluminoborosilicate glasses with varying boron content, Geochim. Cosmochim. Acta **268**, 325 (2020).

[87] Y. S. Yi and S. K. Lee, Pressure-induced changes in local electronic structures of SiO_2 and $MgSiO_3$ polymorphs: Insights from ab initio calculations of O K-edge energy-loss near-edge structure spectroscopy, Am. Mineral. **97**, 897 (2012).